ACS APPLIED MATERIALS & INTERFACES

www.acsami.org Research Article

3D Printed Nickel−Molybdenum-Based Electrocatalysts for Hydrogen Evolution at Low Overpotentials in a Flow-Through Configuration

Ian Sullivan, Huanlei Zhang, Cheng Zhu, Marissa Wood, Art J. Nelson, Sarah E. Baker, Christopher M. Spadaccini, Tony Van Buuren, Meng Lin,* Eric B. Duoss,* Siwei Liang,* and Chengxiang Xiang*

Cite This: *ACS Appl. Mater. Interfaces* 2021, 13, 20260−20268

Read Online

ACCESS | Metrics & More | Article Recommendations | Supporting Information

ABSTRACT: Three-dimensional (3D) printed, hierarchically porous nickel molybdenum (NiMo) electrocatalysts were synthesized and evaluated in a flow-through configuration for the hydrogen evolution reaction (HER) in 1.0 M KOH(aq) in a simple electrochemical H-cell. 3D NiMo electrodes possess hierarchically porous structures because of the resol-based aerogel precursor, which generates superporous carbon aerogel as a catalyst support. Relative to a traditional planar electrode configuration, the flow-through configuration allowed efficient removal of the hydrogen bubbles from the catalyst surface, especially at high operating current densities, and significantly decreased the overpotentials required for HER. An analytical model that accounted for the electrokinetics of HER as well as the mass transport with or without the flow-through configuration was developed to quantitatively evaluate voltage losses associated with kinetic overpotentials and ohmic resistance due to bubble formation in the porous electrodes. The chemical composition, electrochemical surface area (ECSA), and roughness factor (RF) were also systematically studied to assess the electrocatalytic performance of the 3D printed, hierarchically porous NiMo electrodes. An ECSA of 25163 cm^2 was obtained with the highly porous structures, and an average overpotential of 45 mV at 10 mA cm^{-2} was achieved over 24 h by using the flow-through configuration. The flow-through configuration evaluated in the simple H-cell achieved high electrochemical accessible surface areas for electrochemical reactions and provided useful information for adaption of the porous electrodes in flow cells.

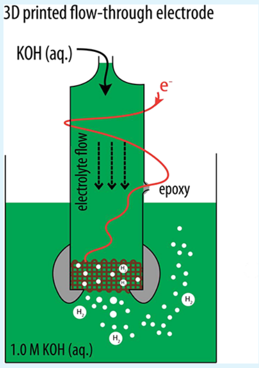

KEYWORDS: *hydrogen evolution reaction, electrocatalysis, 3D printing, alkaline electrolysis, NiMo, flow-through, electrochemistry, solar fuel*

INTRODUCTION

Hydrogen is one of the most promising sources of energy carriers for renewables and has been a focal point of clean energy research in recent years.[1−10] Photoelectrochemical (PEC) and electrochemical approaches for hydrogen production from water electrolysis have advanced significantly in terms of conversion efficiency and stability.[11] Extreme pH environment (e.g., pH = 0 or pH = 14) is the preferred reaction condition for the water-splitting reaction due to the high conductivity of the electrolyte, low polarization loss associated with electrodialysis, and readily available polymer electrolyte membranes, such as cation exchange membrane (CEM) and anion exchange membrane (AEM). In the acidic condition, platinum group metals (PGMs) including Pt, Ir, and Ru are the most common electrocatalysts used to produce hydrogen in commercially available electrolyzers.[3,6,12−14] A main advantage of using PGMs is the low overpotential for the hydrogen evolution reaction (HER). Previous reports of ∼15−80 mV overpotential ranges have been recorded for HER at relevant current densities (10 mA cm^{-2}) and are attributed to favorable kinetics at the electrode surface.[15,16] Pt and IrO_x are often used as the active materials in polymer−electrolyte−membrane (PEM) electrolysis systems operating at >1 A cm^{-2}.[17] While PGMs exhibit excellent catalytic activity for HER, the cost for these materials remains high.[4,11] In the alkaline condition, low-cost, earth-abundant materials such as nickel molybdenum (NiMo) for HER or NiFeOx for oxygen evolution reaction (OER) exhibit excellent activity and stability, with several promising Ni-based materials listed in Table 1.[16,18−22] In particular, NiMo alloys have shown the most promise with overpotentials <50 mV and in some cases lower than PGMs in alkaline conditions.[1,16,20,23−31] NiMo alloys are typically formed by electrodeposition or through drop-casting of presynthesized catalyst inks onto conductive surfaces.[5,29,32] Performance of these films is highly dependent

Received: March 26, 2021
Accepted: April 12, 2021
Published: April 22, 2021

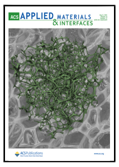

Table 1. State-of-the-Art NiMo-Based Electrodes for Hydrogen Evolution

material	overpotential (mV) 10 mA cm^{-2}	electrolyte	stability (h)	ECSA (cm^2)	flow-through	ref
$MoNi_4$	15	1 M KOH	10	55500	no	25
Mo@MoNi	18	1 M KOH	1680	16750	no	31
NiMo	30	1 M KOH	20	735	no	28
Ni−Zn−CoO	53	6 M KOH	24	N/A	no	24
NiMo nanopowder	70	2 M KOH	96	130	no	16
Mo−Ni	38	1 M KOH	10	N/A	no	20
NiMo (a)	30	1 M NaOH	24	157[a]	no	1
NiMo (b)	130	1 M NaOH	24	196[a]	no	1
NiMoCo	110	1 M NaOH	24	177[a]	no	1
NiMoFe (a)	130	1 M NaOH	24	177[a]	no	1
NiFe	120	1 M NaOH	24	785[a]	no	1
amine modulated NiMo	72	1 M KOH	N/A	N/A	no	29
3D printed NiMo (high Mo)	45	1 M KOH	24	25163	yes	this work

[a] Calculated from multiplying the reported 2D roughness factor (RF) values by geometric area of catalyst on 5 mm diameter glassy carbon disc electrodes.

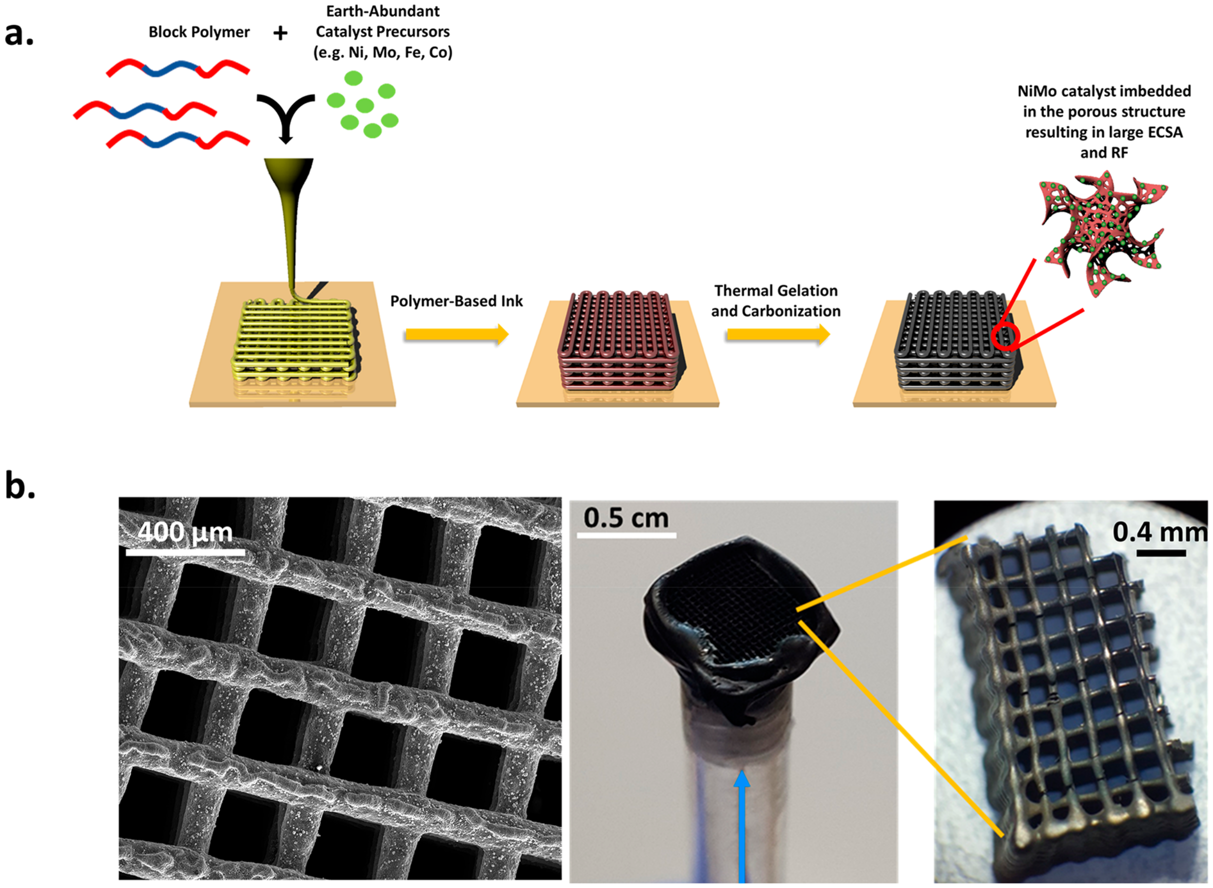

Figure 1. (a) Schematic illustration of the process flow to produce 3D NiMo-based electrocatalysts. (b) Scanning electron microscopy (SEM) image (left) and optical images of NiMo electrocatalysts. The blue arrow indicates the flow of electrolyte.

on the surface area and morphology of the electrode. For instance, hierarchically structured surfaces result in electrodes with increased current density at a given overpotential for water splitting due to large electrochemically active surface areas (ECSA).[28−31] Rotating disc electrodes (RDE) are often used to probe the intrinsic electrocatalytic performance of the material without any mass transport limitations at relatively low current densities.[33−35] Electrochemical flow cells are often employed to overcome mass transport limitations including bubble removal and enhanced ECSAs to achieve high operating current densities.[36,37] Many different flow configurations and strategies were reported to achieve efficient bubble removal for high water-splitting performances.[38−43] For instance, in catalyst bonded membrane cells, such as PEM electrolysis, the flow of purified water steam in the anode chamber is along the width of membrane and along the surface of the porous catalyst layers.[41] In addition, membrane-less, flow-through electrodes employed forced liquid flow orthogonal to the surface of the porous catalyst electrodes and provided a high rate of reactions and product separations.[42,43]

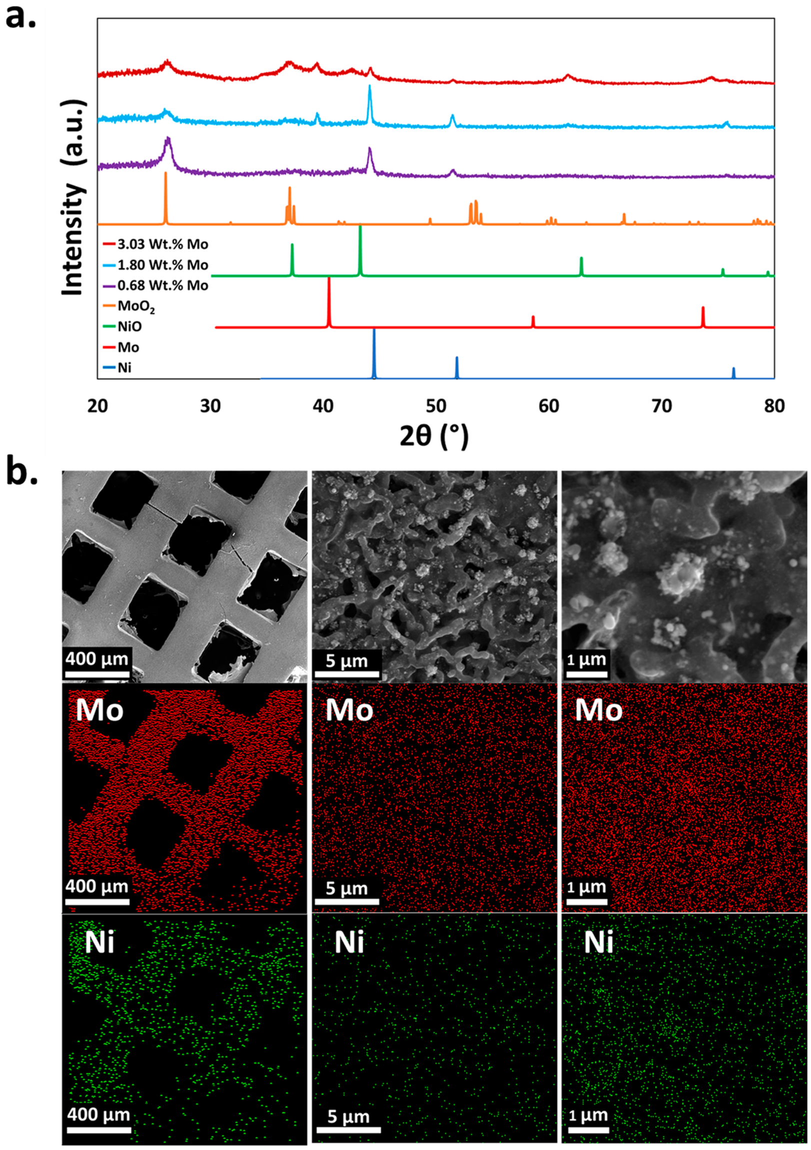

Figure 2. (a) XRD patterns and (b) SEM/EDS of the 3D printed, porous NiMo electrodes.

In this study, we fabricated flow-through electrodes, in which the electrolyte flow direction was orthogonal to the surface of the porous electrode in a simple electrochemical H-cell configuration to evaluate the HER performance for NiMo-based electrocatalysts.

Recently, resorcinol−formaldehyde sol−gel chemistry has proven to be an efficient approach to produce carbon aerogels with superhigh surface areas.[44] By combining versatile fabrication processes such as additive manufacturing (AM) or 3D printing with postprocessing methods such as thermal activation, Chandrasekaran et al. produced 3D carbon aerogels with surface areas ~2000 m^2/g.[45] In other work, Liu et al. leveraged triblock copolymer (Pluronic F127) as a sacrificial template for resol-based polymer to demonstrate ordered mesoporous carbon with high surface area.[46] Printable ink formulations were also developed successfully with multiple inorganic salts and multicomponent metal oxides were synthesized by inkjet printing for quick screening of photocatalytic HER catalysts.[47] Ambrosi et al. have also reported electrodeposition of Ni-based electrocatalysts on 3D printed electrode scaffolds, achieving a high-throughput method of testing catalysts for water splitting.[48] Several previous reports have shown enhanced catalytic activity due to increased ECSA values in the flow-through configuration for different electrochemical reactions (Table S6).[22,49−52]

Herein, we report a 3D printed, hierarchically porous NiMo-based electrocatalyst to dramatically increase the ECSA and roughness factor (RF) and hence lower the overpotentials for HER. Large ECSA and RF values were accessible which can be attributed to the 3D hierarchically porous structure, resulting in the lower overpotentials achieved. A flow-through configuration was employed to reduce mass-transport limitations and efficiently remove bubbles from the surface of the electrode, which could lead to larger overpotentials. Relative to a traditional planar, static electrode configuration, the flow-through configuration allowed efficient removal of hydrogen bubbles from the catalyst surface, especially at high operating current densities, and significantly decreased the overpotentials required for HER. An analytical model that accounts for the electrokinetics of HER as well as the mass transport with or without the flow-through configuration has been developed to quantitatively evaluate various factors for the reduced over-

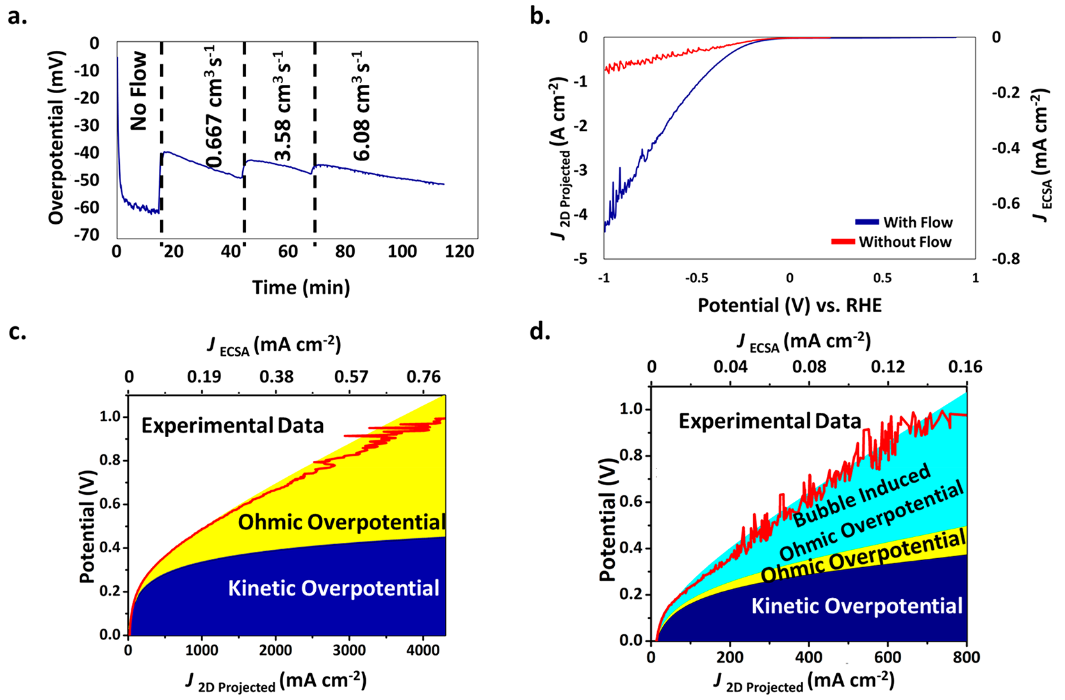

Figure 3. (a) Impact of flow rate on the overpotential of the 3D printed, porous electrodes at $J_{2D,projected}$ = 10 mA cm^{-2} as a function of time. (b) $J_{2D,projected}$ (left axis) and $J_{3D,ECSA}$ (right axis) of the porous NiMo electrodes as a function of the potential vs RHE in a traditional electrode configuration (red) and in a flow-through configuration at a flow rate of 3.58 cm^3 s^{-1} (blue). (c) Simulated contribution from kinetic overpotential and ohmic resistive loss in the flow-through configuration and (d) simulated contribution from kinetic overpotential, ohmic resistive loss, and additional bubble induced ohmic resistive loss in the traditional electrode configuration. The experimental data curves in (c) and (d) are the experimental measurements from (b).

potentials. Bubble-induced ohmic loss accounted for most of the voltage loss at high operating current densities. We have also developed several optimization strategies to control the ink formulation and related elemental compositions of our electrochemical catalysts to reduce reaction overpotentials.

■ RESULTS AND DISCUSSION

Figure 1a shows a schematic illustration of the process flow for ink formulation, 3D printing, sol−gelation, and carbonization steps to create 3D NiMo-based electrocatalysts for use in a flow-through mode. The 3D orderly structure here provided an improved mass flow control as in a flow-through configuration (Figure 1b). The sol−gel process and the following carbonization allowed us to fabricate a hierarchically porous structure with high surface area as demonstrated by SEM images in Figure 2.

X-ray diffraction (XRD) patterns of the prepared substrates, shown in Figure 2a, indicate mixed phases of Ni and MoO_2 for all tested compositions. At a composition of 0.68 wt % Ni and MoO_2 peaks are present in the XRD patterns. As the Mo precursor content increases to 1.8 and 3.03 wt %, NiO and MoO_2 peaks intensify and the cubic Mo phase is observed. In addition, the Mo peaks are shifted to larger 2θ values, indicating possible Ni−Mo alloy formation or solid solutions of the oxide phases (i.e., $Ni_{1-x}Mo_xO_y$).[53−55] We note that the bulk of the electrode is carbon; however, crystalline carbon phases (e.g., graphite) were not observed by XRD, which indicates the carbon is amorphous. X-ray photoelectron spectroscopy (XPS) measurements of NiMo electrodes exhibit peaks for oxidized phases of Ni and Mo at the surface. Depth profiling of the electrode surface revealed a decrease in the satellite peaks of Ni and Mo oxides, with predominant contributions from the Ni^0/Mo^0 increasing with depth, in agreement with the observed phases by XRD measurements (see Figure S3). Tabulated atomic compositions also exhibit lower Mo for low loading NiMo (see Table S1) and increased Mo content for high loading NiMo (Table S4).

Rough, porous surface features and nodules were observed via scanning electron microscopy (SEM) images (Figure 2b), while energy dispersive X-ray spectroscopy (EDX) mapping revealed Mo and Ni compositions dispersed throughout the bulk of the electrode (Figure 2). Upon closer inspection of the surface, increased Ni concentration was discovered in the nodules compared to the rest of the electrode (Figure S4). While Ni and Mo elemental compositions are found to be well dispersed throughout the electrode interior, the increased Ni content of the surface nodules and existence of several phases imply phase segregation. This porous morphology resulted in large ECSAs, as well as very large roughness factors (RF), which is the ratio of ECSA and geometric surface area (see the Supporting Information for calculations).

Flow-through electrodes using 3D printed NiMo substrates were fabricated and measured as detailed in the Supporting Information. After the electrode was immersed in 1 M KOH electrolyte, several flow rates were tested at $J_{2D,projected}$ = 10 mA cm^{-2}. As shown in Figure 3a, an overpotential of 60 mV was measured without electrolyte flow. The observed measurement was noisy due to the formation of H_2 gas bubbles on the surface of the electrode. As the flow started, bubbles immediately left the surface and the overpotential decreased to ∼40 mV, which then slowly increased with time. Further increases in flow rate from 0.667 to 3.58 cm^3 s^{-1} and from 3.58 to 6.08 cm^3 s^{-1} had a much smaller impact on the overpotential of the reaction. Therefore, we used a flow rate

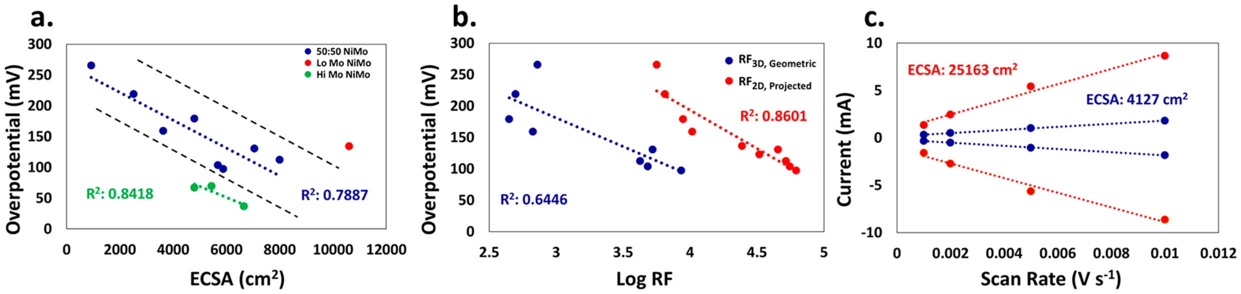

Figure 4. (a) Overpotential at $J_{2D,projected}$ = 10 mA cm^{-2} as a function of ECSA and Mo content. (b) Correlation between the overpotential at $J_{2D,projected}$ = 10 mA cm^{-2} and $RF_{3D,geometric}$ (blue) and $RF_{2D,projected}$ (red). (c) ECSA values before (blue) and after (red) electrochemical oxidation.

of 3.58 cm^3 s^{-1} in all flow-through measurements. Linear sweep voltammetry (LSV) measurements were performed with and without flow to determine mass transport limitations of the electrodes, as shown in Figure 3b. Stark differences were observed with or without electrolyte flow, especially at high operating current densities. For example, at $J_{2D,projected}$ = 500 mA cm^{-2} an overpotential of −0.36 and −0.77 V was obtained with and without flow, respectively. The flow-through electrode also allowed much higher current densities to be achieved without reaching the mass transport limiting current density.

An analytical model that accounted for the electrokinetics as well as mass transport was developed to quantitatively understand the current−voltage characteristics of the electrode with or without electrolyte flow. In this study, the electrolyte flow direction was orthogonal to the surface of the porous electrodes, and given the size of the porous electrode was in the range 0.1−0.2 cm^2 (see the Supporting Information for detailed measurements), we do not anticipate any large spatial variation of the current density along the surface of the electrodes. In the traditional electrode configuration without convective electrolyte flow, the generated hydrogen bubbles adhere to the electrode surface and reduce the ECSA for HER. In addition, the coverage of bubbles can also cause the electrolyte resistance to increase, especially operating at high current densities. As a result, the bubble coverage in the porous electrode can directly affect the ohmic resistive loss and kinetic overpotential in the system.[56] The total voltage drop (U) of the catalytic electrodes at a given operating current density is the sum of the kinetic overpotential (η) and the ohmic overpotentials due to electrolyte resistance (R_0) and bubble-induced resistance (R_{bubble}):

$$U = \eta + IR_0 + IR_{bubble} \tag{1}$$

The kinetic overpotential, η, was assumed a Tafel relation as the following:

$$j = j_0(1 - \Theta)\exp\left(\frac{\alpha zF\eta}{RT}\right) \tag{2}$$

where $j_0(1 - \Theta)$ denotes the bubble-affected exchange current density. j_0 is the exchange current density of the flow-through case (6.32 mA cm^{-2} when $\Theta = 0$). α is the transfer coefficient, z is the transfer charge number in reaction, F is Faraday's constant, R is a gas constant, and T is the temperature, which is equal to 25 °C. The Tafel relation was then rewritten into the following format:

$$\eta = a + b\log(j) \tag{3}$$

where $a = -(2.303RT/\alpha zF)\cdot\log[j_0(1 - \Theta)]$ and $b = 2.303RT/\alpha zF$. The fitted α is 0.196 based on our experiment data for the flow-through configuration leading to Tafel slope b = 185.6 mV per decade of current density.

For the porous electrodes without any flow, Θ was determined according to the operation current density, j, based on the following correlation:[57]

$$\frac{j}{J_{max}} = 3.08\Theta^{1.5}(1 - \Theta)^{0.5} \tag{4}$$

where J_{max} represents the maximum current density, which is empirically chosen to correlate with the experimental data. The value of J_{max} was set to 1000 mA cm^{-2} in the calculation. Note that in the simulation all the current densities, including the exchange current density, j_0, and the maximum current density, J_{max}, were normalized to the 2D projected surface areas to compare with the experimental results. Both the experimental results and the modeling results were also plotted when the current density was normalized to the 3D, ECSA of the porous electrodes in Figure 3.

In the flow-through configuration without any hydrogen bubble buildup, the resistance (R_0) can be assumed to be a fixed value and equal to 0.88 Ω, and R_{bubble} is based on the experimental data, which was found to be 4.15 Ω in this study. As shown in Figure 3d, the ohmic resistive loss becomes the dominating factor at an operating current density $J_{2D,projected}$ > ∼200 mA cm^2 in the flow-through configuration. At $J_{2D,projected}$ = 500 mA cm^{-2}, the kinetic overpotential increased from ∼285 to ∼310 mV due to the reduction of the ECSA when the electrolyte flow stopped, and the ohmic resistive loss due to bubble formation was ∼360 mV, which accounted for the majority of the voltage drop in the traditional planar electrode configuration.

A range of chemical compositions and ECSAs of the porous electrodes were evaluated in the flow-through configuration at an operating current density of $J_{2D,projected}$ = 10 mA cm^{-2}. Both ECSA and Mo content impacted the overpotential for HER as shown in Figure 4a, and as the ECSA was increased, a decrease in overpotential was observed. It was also observed that increased Mo content decreased the overpotential as well, with three distinct regions outlined. Higher Mo content electrodes achieved the lowest overpotentials, while low Mo content electrodes resulted in larger overpotentials, even with high ECSA values. The improved catalytic performance in high Mo content electrodes agrees well with previous reports.[16,32] To further understand the correlation between Mo content and overpotential, electrochemical impedance spectroscopy (EIS) measurements were performed with increasing amounts of Mo content; however, we did not observe any correlations between

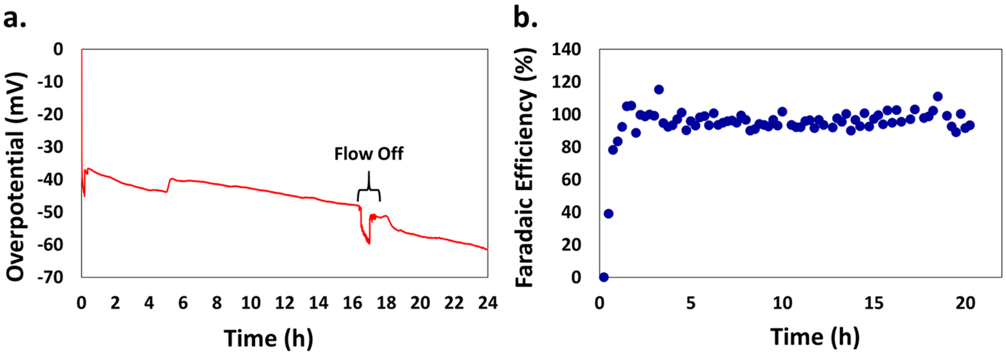

Figure 5. (a) Chronopotentiometry (CP) measurements of NiMo electrode at $J_{2D,projected}$ = 10 mA cm^{-2} for 24 h and (b) the corresponding Faradaic efficiency for hydrogen generation.

Mo content or resistivity (Figure S5 and Table S3). We then focused our efforts on understanding the impacts of porosity on overpotential. Several previous reports have shown enhanced catalytic activity due to increased ECSA and RF values and have achieved low overpotentials for HER and enhanced current densities for carbon conversion. Control experiments with 3D printed carbon electrodes (without NiMo) and flat NiMo electrodes without a flow-through configuration resulted in larger overpotentials of 524 and 209 mV, respectively (see Table S1). In the high Mo content electrodes, the ECSA of the porous electrodes was systematically varied by increasing the number of 3D printed layers or by changing the flow-through channel sizes (Figure S6).

The overpotential at $J_{2D,projected}$ = 10 mA cm^{-2} was investigated as a function of the roughness factor (RF) as shown in Figure 4b. The $RF_{2D,projected}$ and $RF_{3D,geometric}$ were defined as the following:

$$RF_{2D,projected} = \frac{\text{ECSA}}{\text{2D projected surface area}} \quad (5)$$

$$RF_{3D,geometric} = \frac{\text{ECSA}}{\text{3D geometric surface area}} \quad (6)$$

The detailed estimations of the 2D projected surface area and the 3D geometric surface area are provided in the Supporting Information. The overpotential at $J_{2D,projected}$ = 10 mA cm^{-2} exhibited a strong inverse linear correlation with the $RF_{2D,projected}$, while exhibiting a weaker linear fit with $RF_{3D,geometric}$. After observing the trends between ECSA and overpotential, we decided to perform electrochemical surface roughening by oxidizing the surface of the electrode through cyclic voltammetry (CV) in 1 M KOH. ECSA measurements were performed by CV scans (Figure S7), and a dramatic increase in the ECSA and RF was observed after oxidation (e.g., ECSA increased by a factor of 6.09) (Figure 4c). Chronopotentiometry (CP) measurements (Figure S8) before and after oxidation of the same electrode showed that the increased ECSA led to lower overpotentials at $J_{2D,projected}$ = 10 mA cm^{-2}. XRD patterns before and after oxidation measurements are nearly identical, indicating that the phases present were not changed by electrochemical oxidation (Figure S9); therefore, we attribute the decrease of overpotential to increased ECSA.

Figure 5 shows the overpotential at $J_{2D,projected}$ = 10 mA cm^{-2} as a function of time using an oxidized high Mo content porous electrode in a flow-through configuration. For the initial 12 h, the measured overpotential was <50 mV, which gradually increased to ~70 mV after 24 h as shown in Figure 5a. An average overpotential of ~45 mV was observed during this 24 h testing period. During this period, an average H_2 Faradaic yield of 96% (±5%) was measured by gas chromatography (GC), indicating that the sole reaction was HER, with no observed side reactions (e.g., oxide reduction) (Figure 5b). The measurement was performed for a total of 116 h, over which time the overpotential gradually increased to 122 mV (Figure S10).

CONCLUSION

In summary, 3D printed, porous NiMo-based electrodes were evaluated in a flow-through configuration for the hydrogen evolution reaction (HER) in 1.0 M KOH in a simple electrochemical H-cell. The 3D printed electrodes exhibit uniform chemical composition with complex, multiscale interior, and surface structure, which lead to high roughness factors (RFs) and high electrochemically accessible surface areas, especially under high operating current densities. The current density−voltage characteristics of the same electrode in the traditional electrode configuration and in the flow-through electrode configuration were compared side-by-side, and the current density−voltage behavior was fitted by an analytical model that accounted for electrokinetics and mass transport within the porous electrodes. The efficient hydrogen bubble removal from the electrode surface lowered the losses associated with kinetic overpotentials and ohmic resistances when comparing against a traditional flat electrode configuration. The simulation results also showed that the bubble induced resistive loss was the largest voltage loss in the traditional electrode configuration, especially under high operating current densities. While the intrinsic catalytic performance of the prepared NiMo catalyst was moderate, when the catalyst was employed in a flow-through configuration to reduce mass-transport loss and efficiently remove surface bubbles, an average overpotential of 45 mV at $J_{2D,projected}$ = 10 mA cm^{-2} was realized over 24 h. This simple flow-through configuration in an electrochemical H-cell provided useful information for adaption of the porous electrodes in flow cells.

ASSOCIATED CONTENT

Supporting Information

The Supporting Information is available free of charge at https://pubs.acs.org/doi/10.1021/acsami.1c05648.

Experimental methods for resin synthesis, electrode fabrication, materials characterization, electrochemical measurements, electrochemical oxidations, ECSA measurements, SEM images, EDX, XRD, and gas chromatography (PDF)

AUTHOR INFORMATION

Corresponding Authors

Chengxiang Xiang − *Liquid Sunlight Alliance (LiSA), and Department of Applied Physics and Material Science, California Institute of Technology, Pasadena, California 91125, United States;* orcid.org/0000-0002-1698-6754; Email: cxx@caltech.edu

Siwei Liang − *Lawrence Livermore National Laboratory, Livermore, California 94550, United States;* Email: liang11@llnl.gov

Eric B. Duoss − *Lawrence Livermore National Laboratory, Livermore, California 94550, United States;* Email: duoss1@llnl.gov

Meng Lin − *Department of Mechanical and Energy Engineering, Southern University of Science and Technology, Shenzhen, Guangdong 518055, China;* orcid.org/0000-0001-7785-749X; Email: linm@sustech.edu.cn

Authors

Ian Sullivan − *Liquid Sunlight Alliance (LiSA), and Department of Applied Physics and Material Science, California Institute of Technology, Pasadena, California 91125, United States;* orcid.org/0000-0003-0632-4607

Huanlei Zhang − *Department of Mechanical and Energy Engineering, Southern University of Science and Technology, Shenzhen, Guangdong 518055, China*

Cheng Zhu − *Lawrence Livermore National Laboratory, Livermore, California 94550, United States;* orcid.org/0000-0003-0084-1099

Marissa Wood − *Lawrence Livermore National Laboratory, Livermore, California 94550, United States*

Art J. Nelson − *Lawrence Livermore National Laboratory, Livermore, California 94550, United States*

Sarah E. Baker − *Lawrence Livermore National Laboratory, Livermore, California 94550, United States*

Christopher M. Spadaccini − *Lawrence Livermore National Laboratory, Livermore, California 94550, United States*

Tony Van Buuren − *Lawrence Livermore National Laboratory, Livermore, California 94550, United States*

Complete contact information is available at:
https://pubs.acs.org/10.1021/acsami.1c05648

Author Contributions

I.S. performed the electrochemical measurements, materials characterization, SEM imaging, and electrode fabrication. S.L. performed synthesis of the resin and NiMo substrates. A.J.N. performed XPS measurements and analysis. All authors contributed to conceptualization of the research and assisted with preparing, writing, and editing the manuscript.

Notes

The authors declare no competing financial interest.

ACKNOWLEDGMENTS

The materials synthesis work at LLNL was performed under the auspices of the US Department of Energy under Contract DE-AC52-07NA27344, and this work was supported by funding from LDRD Awards 19-SI-005 and 19-FS-047 and IM review # LLNL-JRNL-816169. The characterization and analytical calculation of the flow-through electrodes are based on work performed by the Liquid Sunlight Alliance, which is supported by the U.S. Department of Energy, Office of Science, Office of Basic Energy Sciences, Fuels from Sunlight Hub under Award DE-SC0021266.

REFERENCES

(1) McCrory, C. C. L.; Jung, S.; Ferrer, I. M.; Chatman, S. M.; Peters, J. C.; Jaramillo, T. F. Benchmarking Hydrogen Evolving Reaction and Oxygen Evolving Reaction Electrocatalysts for Solar Water Splitting Devices. *J. Am. Chem. Soc.* **2015**, *137* (13), 4347−4357.

(2) Lewis, N. S.; Nocera, D. G. Powering the Planet: Chemical Challenges in Solar Energy Utilization. *Proc. Natl. Acad. Sci. U. S. A.* **2006**, *103* (43), 15729−15735.

(3) Cheng, N.; Stambula, S.; Wang, D.; Banis, M. N.; Liu, J.; Riese, A.; Xiao, B.; Li, R.; Sham, T. K.; Liu, L. M.; Botton, G. A.; Sun, X. Platinum Single-Atom and Cluster Catalysis of the Hydrogen Evolution Reaction. *Nat. Commun.* **2016**, *7*, 1−9.

(4) Eftekhari, A. Electrocatalysts for Hydrogen Evolution Reaction. *Int. J. Hydrogen Energy* **2017**, *42* (16), 11053−11077.

(5) Gong, M.; Wang, D.; Chen, C.; Hwang, B.; Dai, H. A Mini Review on Nickel-Based Electrocatalysts for Alkaline Hydrogen Evolution Reaction. *Nano Res.* **2016**, *9* (1), 28−46.

(6) Grigoriev, S. A.; Millet, P.; Fateev, V. N. Evaluation of Carbon-Supported Pt and Pd Nanoparticles for the Hydrogen Evolution Reaction in PEM Water Electrolysers. *J. Power Sources* **2008**, *177* (2), 281−285.

(7) Jiang, S.; Zhang, R.; Liu, H.; Rao, Y.; Yu, Y.; Chen, S.; Yue, Q.; Zhang, Y.; Kang, Y. Promoting Formation of Oxygen Vacancies in Two-Dimensional Cobalt-Doped Ceria Nanosheets for Efficient Hydrogen Evolution. *J. Am. Chem. Soc.* **2020**, *142* (14), 6461−6466.

(8) Liu, E.; Li, J.; Jiao, L.; Doan, H. T. T.; Liu, Z.; Zhao, Z.; Huang, Y.; Abraham, K. M.; Mukerjee, S.; Jia, Q. Unifying the Hydrogen Evolution and Oxidation Reactions Kinetics in Base by Identifying the Catalytic Roles of Hydroxyl-Water-Cation Adducts. *J. Am. Chem. Soc.* **2019**, *141* (7), 3232−3239.

(9) Mahmood, N.; Yao, Y.; Zhang, J.-W.; Pan, L.; Zhang, X.; Zou, J.-J. Electrocatalysts for Hydrogen Evolution in Alkaline Electrolytes: Mechanisms, Challenges, and Prospective Solutions. *Adv. Sci.* **2018**, *5* (2), 1700464.

(10) Zheng, Y.; Jiao, Y.; Vasileff, A.; Qiao, S. The Hydrogen Evolution Reaction in Alkaline Solution: From Theory, Single Crystal Models, to Practical Electrocatalysts. *Angew. Chem., Int. Ed.* **2018**, *57* (26), 7568−7579.

(11) Ramaswamy, N.; Mukerjee, S. Alkaline Anion-Exchange Membrane Fuel Cells: Challenges in Electrocatalysis and Interfacial Charge Transfer. *Chem. Rev.* **2019**, *119* (23), 11945−11979.

(12) Jiang, P.; Yang, Y.; Shi, R.; Xia, G.; Chen, J.; Su, J.; Chen, Q. Pt-like Electrocatalytic Behavior of Ru-MoO2 Nanocomposites for the Hydrogen Evolution Reaction. *J. Mater. Chem. A* **2017**, *5* (11), 5475−5485.

(13) Stamenkovic, V. R.; Strmcnik, D.; Lopes, P. P.; Markovic, N. M. Energy and Fuels from Electrochemical Interfaces. *Nat. Mater.* **2017**, *16* (1), 57−69.

(14) Yu, J.; Guo, Y.; She, S.; Miao, S.; Ni, M.; Zhou, W.; Liu, M.; Shao, Z. Bigger Is Surprisingly Better: Agglomerates of Larger RuP Nanoparticles Outperform Benchmark Pt Nanocatalysts for the Hydrogen Evolution Reaction. *Adv. Mater.* **2018**, *30* (39), 1800047.

(15) Wu, Q.; Luo, M.; Han, J.; Peng, W.; Zhao, Y.; Chen, D.; Peng, M.; Liu, J.; de Groot, F. M. F.; Tan, Y. Identifying Electrocatalytic Sites of the Nanoporous Copper−Ruthenium Alloy for Hydrogen Evolution Reaction in Alkaline Electrolyte. *ACS Energy Lett.* **2020**, *5* (1), 192−199.

(16) McKone, J. R.; Sadtler, B. F.; Werlang, C. A.; Lewis, N. S.; Gray, H. B. Ni−Mo Nanopowders for Efficient Electrochemical Hydrogen Evolution. *ACS Catal.* **2013**, *3* (2), 166−169.

(17) Xu, D.; Stevens, M. B.; Cosby, M. R.; Oener, S. Z.; Smith, A. M.; Enman, L. J.; Ayers, K. E.; Capuano, C. B.; Renner, J. N.; Danilovic, N.; Li, Y.; Wang, H.; Zhang, Q.; Boettcher, S. W. Earth-Abundant Oxygen Electrocatalysts for Alkaline Anion-Exchange-Membrane Water Electrolysis: Effects of Catalyst Conductivity and Comparison with Performance in Three-Electrode Cells. *ACS Catal.* **2019**, *9* (1), 7−15.

(18) Lu, X.; Zhao, C. Electrodeposition of Hierarchically Structured Three-Dimensional Nickel−Iron Electrodes for Efficient Oxygen Evolution at High Current Densities. *Nat. Commun.* **2015**, *6* (1), 6616.

(19) McCrory, C. C. L.; Jung, S.; Peters, J. C.; Jaramillo, T. F. Benchmarking Heterogeneous Electrocatalysts for the Oxygen Evolution Reaction. *J. Am. Chem. Soc.* **2013**, *135* (45), 16977−16987.

(20) Zhou, Y.; Luo, M.; Zhang, W.; Zhang, Z.; Meng, X.; Shen, X.; Liu, H.; Zhou, M.; Zeng, X. Topological Formation of a Mo-Ni-Based Hollow Structure as a Highly Efficient Electrocatalyst for the Hydrogen Evolution Reaction in Alkaline Solutions. *ACS Appl. Mater. Interfaces* **2019**, *11*, 21998.

(21) Zeng, M.; Li, Y. Recent Advances in Heterogeneous Electrocatalysts for the Hydrogen Evolution Reaction. *J. Mater. Chem. A* **2015**, *3* (29), 14942−14962.

(22) Merki, D.; Vrubel, H.; Rovelli, L.; Fierro, S.; Hu, X. Fe, Co, and Ni Ions Promote the Catalytic Activity of Amorphous Molybdenum Sulfide Films for Hydrogen Evolution. *Chem. Sci.* **2012**, *3* (8), 2515−2525.

(23) Pehlivan, İ. B.; Arvizu, M. A.; Qiu, Z.; Niklasson, G. A.; Edvinsson, T. Impedance Spectroscopy Modeling of Nickel−Molybdenum Alloys on Porous and Flat Substrates for Applications in Water Splitting. *J. Phys. Chem. C* **2019**, *123* (39), 23890−23897.

(24) Ling, T.; Zhang, T.; Ge, B.; Han, L.; Zheng, L.; Lin, F.; Xu, Z.; Hu, W.; Du, X.; Davey, K.; Qiao, S. Well-Dispersed Nickel- and Zinc-Tailored Electronic Structure of a Transition Metal Oxide for Highly Active Alkaline Hydrogen Evolution Reaction. *Adv. Mater.* **2019**, *31* (16), 1807771.

(25) Zhang, J.; Wang, T.; Liu, P.; Liao, Z.; Liu, S.; Zhuang, X.; Chen, M.; Zschech, E.; Feng, X. Efficient Hydrogen Production on $MoNi_4$ Electrocatalysts with Fast Water Dissociation Kinetics. *Nat. Commun.* **2017**, *8* (May), 1−8.

(26) Chen, W.; Sasaki, K.; Ma, C.; Frenkel, A. I.; Marinkovic, N.; Muckerman, J. T.; Zhu, Y.; Adzic, R. R. Hydrogen-Evolution Catalysts Based on Non-Noble Metal Nickel-Molybdenum Nitride Nanosheets. *Angew. Chem., Int. Ed.* **2012**, *51* (25), 6131−6135.

(27) Fan, C.; Piron, D. L.; Sleb, A.; Paradis, P. Study of Electrodeposited Nickel-Molybdenum, Cobalt-Tungsten as Hydrogen Electrodes in Alkaline Water Electrolysis. *J. Electrochem. Soc.* **1994**, *141* (2), 382−387.

(28) Fang, M.; Gao, W.; Dong, G.; Xia, Z.; Yip, S.; Qin, Y.; Qu, Y.; Ho, J. C. Hierarchical NiMo-Based 3D Electrocatalysts for Highly-Efficient Hydrogen Evolution in Alkaline Conditions. *Nano Energy* **2016**, *27*, 247−254.

(29) Gao, W.; Gou, W.; Zhou, X.; Ho, J. C.; Ma, Y.; Qu, Y. Amine-Modulated/Engineered Interfaces of NiMo Electrocatalysts for Improved Hydrogen Evolution Reaction in Alkaline Solutions. *ACS Appl. Mater. Interfaces* **2018**, *10* (2), 1728−1733.

(30) Ito, Y.; Ohto, T.; Hojo, D.; Wakisaka, M.; Nagata, Y.; Chen, L.; Hu, K.; Izumi, M.; Fujita, J.; Adschiri, T. Cooperation between Holey Graphene and NiMo Alloy for Hydrogen Evolution in an Acidic Electrolyte. *ACS Catal.* **2018**, *8* (4), 3579−3586.

(31) Liu, Z.; Zhang, G.; Bu, J.; Ma, W.; Yang, B.; Zhong, H.; Li, S.; Wang, T.; Zhang, J. Single-Crystalline Mo-Nanowire-Mediated Directional Growth of High-Index-Faceted MoNi Electrocatalyst for Ultralong-Term Alkaline Hydrogen Evolution. *ACS Appl. Mater. Interfaces* **2020**, *12* (32), 36259−36267.

(32) Navarro-Flores, E.; Chong, Z.; Omanovic, S. Characterization of Ni, NiMo, NiW and NiFe Electroactive Coatings as Electrocatalysts for Hydrogen Evolution in an Acidic Medium. *J. Mol. Catal. A: Chem.* **2005**, *226* (2), 179−197.

(33) Arminio-Ravelo, J. A.; Jensen, A. W.; Jensen, K. D.; Quinson, J.; Escudero-Escribano, M. Electrolyte Effects on the Electrocatalytic Performance of Iridium-Based Nanoparticles for Oxygen Evolution in Rotating Disc Electrodes. *ChemPhysChem* **2019**, *20* (22), 2956−2963.

(34) Mayrhofer, K. J. J.; Strmcnik, D.; Blizanac, B. B.; Stamenkovic, V.; Arenz, M.; Markovic, N. M. Measurement of Oxygen Reduction Activities via the Rotating Disc Electrode Method: From Pt Model Surfaces to Carbon-Supported High Surface Area Catalysts. *Electrochim. Acta* **2008**, *53* (7), 3181−3188.

(35) Zhu, P.; Zhao, Y. Effects of Electrochemical Reaction and Surface Morphology on Electroactive Surface Area of Porous Copper Manufactured by Lost Carbonate Sintering. *RSC Adv.* **2017**, *7* (42), 26392−26400.

(36) Fuller, T.; Harb, J. *Electrochemical Engineering*; John Wiley & Sons, Inc.: 2018.

(37) Landolt, D. Flow Channel Cell Apparatus for High Rate Electrolysis Studies. *Rev. Sci. Instrum.* **1972**, *43* (4), 592−595.

(38) Yang, F.; Kim, M. J.; Brown, M.; Wiley, B. J. Alkaline Water Electrolysis at 25 A cm^{-2} with a Microfibrous Flow-through Electrode. *Adv. Energy Mater.* **2020**, *10* (25), 2001174.

(39) Sandeep, K. C.; Kamath, S.; Mistry, K.; Kumar M, A.; Bhattacharya, S. K.; Bhanja, K.; Mohan, S. Experimental Studies and Modeling of Advanced Alkaline Water Electrolyser with Porous Nickel Electrodes for Hydrogen Production. *Int. J. Hydrogen Energy* **2017**, *42* (17), 12094−12103.

(40) Vogt, H.; Balzer, R. J. The Bubble Coverage of Gas-Evolving Electrodes in Stagnant Electrolytes. *Electrochim. Acta* **2005**, *50* (10), 2073−2079.

(41) Carmo, M.; Fritz, D. L.; Mergel, J.; Stolten, D. A Comprehensive Review on PEM Water Electrolysis. *Int. J. Hydrogen Energy* **2013**, *38* (12), 4901−4934.

(42) Gillespie, M. I.; Kriek, R. J. Hydrogen Production from a Rectangular Horizontal Filter Press Divergent Electrode-Flow-Through ($DEFT^{TM}$) Alkaline Electrolysis Stack. *J. Power Sources* **2017**, *372*, 252−259.

(43) Gillespie, M. I.; Van Der Merwe, F.; Kriek, R. J. Performance Evaluation of a Membraneless Divergent Electrode-Flow-through (DEFT) Alkaline Electrolyser Based on Optimisation of Electrolytic Flow and Electrode Gap. *J. Power Sources* **2015**, *293*, 228−235.

(44) Baumann, T. F.; Worsley, M. A.; Han, T. Y. J.; Satcher, J. H. High Surface Area Carbon Aerogel Monoliths with Hierarchical Porosity. *J. Non-Cryst. Solids* **2008**, *354* (29), 3513−3515.

(45) Chandrasekaran, S.; Yao, B.; Liu, T.; Xiao, W.; Song, Y.; Qian, F.; Zhu, C.; Duoss, E. B.; Spadaccini, C. M.; Li, Y.; Worsley, M. A. Direct Ink Writing of Organic and Carbon Aerogels. *Mater. Horiz.* **2018**, *5* (6), 1166−1175.

(46) Liu, R.; Shi, Y.; Wan, Y.; Meng, Y.; Zhang, F.; Gu, D.; Chen, Z.; Tu, B.; Zhao, D. Triconstituent Co-Assembly to Ordered Mesostructured Polymer-Silica and Carbon-Silica Nanocomposites and Large-Pore Mesoporous Carbons with High Surface Areas. *J. Am. Chem. Soc.* **2006**, *128* (35), 11652−11662.

(47) Liu, X.; Shen, Y.; Yang, R.; Zou, S.; Ji, X.; Shi, L.; Zhang, Y.; Liu, D.; Xiao, L.; Zheng, X.; Li, S.; Fan, J.; Stucky, G. D. Inkjet Printing Assisted Synthesis of Multicomponent Mesoporous Metal Oxides for Ultrafast Catalyst Exploration. *Nano Lett.* **2012**, *12* (11), 5733−5739.

(48) Ambrosi, A.; Pumera, M. Multimaterial 3D-Printed Water Electrolyzer with Earth-Abundant Electrodeposited Catalysts. *ACS Sustainable Chem. Eng.* **2018**, *6* (12), 16968−16975.

(49) Inaba, M.; Jensen, A. W.; Sievers, G. W.; Escudero-Escribano, M.; Zana, A.; Arenz, M. Benchmarking High Surface Area Electrocatalysts in a Gas Diffusion Electrode: Measurement of Oxygen Reduction Activities under Realistic Conditions. *Energy Environ. Sci.* **2018**, *11* (4), 988−994.

(50) Herraiz-Cardona, I.; Ortega, E.; Antón, J. G.; Pérez-Herranz, V. Assessment of the Roughness Factor Effect and the Intrinsic Catalytic Activity for Hydrogen Evolution Reaction on Ni-Based Electrodeposits. *Int. J. Hydrogen Energy* **2011**, *36* (16), 9428−9438.

(51) Murthy, A. P.; Theerthagiri, J.; Madhavan, J.; Murugan, K. Highly Active MoS_2/Carbon Electrocatalysts for the Hydrogen Evolution Reaction - Insight into the Effect of the Internal Resistance and Roughness Factor on the Tafel Slope. *Phys. Chem. Chem. Phys.* **2017**, *19* (3), 1988−1998.

(52) Han, L.; Zhou, W.; Xiang, C. High-Rate Electrochemical Reduction of Carbon Monoxide to Ethylene Using Cu-Nanoparticle-Based Gas Diffusion Electrodes. *ACS Energy Lett.* **2018**, *3* (4), 855−860.

(53) Shang, P.; Ye, Z.; Ding, Y.; Zhu, Z.; Peng, X.; Ma, G.; Li, D. Nanosponge-like Solid Solution of NiMo with a High Hydrogen Evolution Reaction Performance over a Wide Range of Current Densities. *ACS Sustainable Chem. Eng.* **2020**, *8* (29), 10664−10672.

(54) Nairan, A.; Zou, P.; Liang, C.; Liu, J.; Wu, D.; Liu, P.; Yang, C. NiMo Solid Solution Nanowire Array Electrodes for Highly Efficient Hydrogen Evolution Reaction. *Adv. Funct. Mater.* **2019**, *29* (44), 1903747.

(55) Liu, J. H.; Pei, Z. L.; Shi, W. B.; Liu, Y. D.; Gong, J.; Sun, C. Studies on Preparation, Microstructure, Mechanical Properties and Corrosion Resistance of Ni[Sbnd]Mo/Micron-Sized Diamond Composite Coatings. *Surf. Coat. Technol.* **2020**, *385*, 125451.

(56) Angulo, A.; van der Linde, P.; Gardeniers, H.; Modestino, M.; Fernández Rivas, D. Influence of Bubbles on the Energy Conversion Efficiency of Electrochemical Reactors. *Joule* **2020**, *4* (3), 555−579.

(57) Vogt, H. The Quantities Affecting the Bubble Coverage of Gas-Evolving Electrodes. *Electrochim. Acta* **2017**, *235*, 495−499.

https://doi.org/10.1021/acsami.1c05648